



Tetragonal CoMn_2O_4 nanocrystals on electrospun carbon fibers as a high-performance battery-type supercapacitor electrode material

Journal:	<i>Dalton Transactions</i>
Manuscript ID	DT-ART-08-2021-002829.R1
Article Type:	Paper
Date Submitted by the Author:	29-Sep-2021
Complete List of Authors:	Mijailovic, Daniel M.; University of Belgrade Faculty of Technology and Metallurgy, Radmilović, Vuk; University of Belgrade Faculty of Technology and Metallurgy, Lacnjevac, Uros; University of Belgrade, Multidisciplinary Research Stojanovic, Dusica; University of Belgrade Faculty of Technology and Metallurgy Bustillo, Karen; Lawrence Berkeley National Lab, Jovic, Vladimir; University of Belgrade Institute for Multidisciplinary Research Radmilović, Velimir; University of Belgrade Faculty of Technology and Metallurgy Uskokovic, Petar; University of Belgrade Faculty of Technology and Metallurgy

ARTICLE

Tetragonal CoMn₂O₄ nanocrystals on electrospun carbon fibers as a high-performance battery-type supercapacitor electrode material

Received 00th January 20xx,
Accepted 00th January 20xx

DOI: 10.1039/x0xx00000x

Daniel M. Mijailović,^a Vuk V. Radmilović,^b Uroš Č. Lačnjevac,^c Dušica B. Stojanović,^b Karen C. Bustillo,^d Vladimir D. Jović,^c Velimir R. Radmilović,^{b,e} and Petar S. Uskoković^{*b}

We herein report a simple two-step procedure for fabricating tetragonal CoMn₂O₄ spinel nanocrystals on carbon fibers. The battery-type behavior of these composite fibers arises from the redox activity of CoMn₂O₄ in an alkaline aqueous solution, which, in combination with the carbon fibers, endows good electrochemical performance and long-term stability. The C@CoMn₂O₄ electrode demonstrated high specific capacity, up to 62 mAh g⁻¹ at 1 A g⁻¹ with capacity retention of around 90% after 4000 cycles. A symmetrical coin-cell device assembled with the composite electrodes delivered high energy density of 7.3 Wh kg⁻¹ at a power density of 0.1 kW kg⁻¹, which is around 13 times higher than that of bare carbon electrodes. The coin cell was cycled for 5000 cycles with 96.3% of capacitance retention, at a voltage of up to 0.8 V, demonstrating excellent cycling stability.

1. Introduction

In past decades, tremendous efforts have been devoted to supercapacitors (SCs) due to their exceptional properties such as high power density, fast charge/discharge rate, very long cycle stability and high safety.¹ The development of this energy storage technology has been mainly focused on increasing the energy density (or specific energy) beyond the current level in order to keep up with advances in portable electronic devices and electric vehicles.² In general, energy density (E_d) might be improved by either capacitance (C) enhancement or voltage (ΔV) expansion:

$$E_d = \frac{1}{2} C \Delta V^2 \quad (1)$$

Activated carbons (ACs) with a well-developed specific surface area (even up to 3500 m² g⁻¹) have been explored over the past decades as the most common electrode materials due to their high electronic conductivity and low cost. Commercial devices are made up of two symmetric AC-based electrodes and organic electrolyte with operating voltages in the range 2.5–2.7 V.

Charge storage of these electric double layer capacitors (EDLCs) occurs directly across the double layer without any charge transfer, thus, providing extremely high-power capability and very long lifetime during charging/discharging (>10⁶ cycles).³

Transition metal (Mn, Ni, Co, *etc.*) oxides have drawn much attention as promising battery-type electrodes for SCs due to their high specific capacity, abundance and low cost.^{4,5} In particular, spinel-type metal oxides with robust crystalline architecture and three-dimensional diffusion pathways could offer high electrochemical activity.⁶ They usually share a common structure although their electrochemical behavior depends on the transition metal(s) involved. Unlike in EDLCs, charges are stored through fast redox reactions. Therefore, spinels express higher capacities than carbons by at least one order of magnitude. Various spinels have been successfully utilized in supercapacitors and lithium-ion batteries with extremely high capacities and good rate capabilities.^{7,8} For example, porous CoMn₂O₄ nanowires with superior electrochemical properties as a supercapacitive electrode have been successfully prepared by thermal decomposition of organometallic compounds.⁹ This electrode exhibits battery-type charge storage due to the formation of oxyhydroxides during charge/discharge processes in an alkaline aqueous electrolyte. Liu *et al.*¹⁰ reported MnCo₂O₄ mesoporous nanowires grown on nickel foam with a high specific capacity and good cycling stability. Chen *et al.*¹¹ designed and synthesized novel hierarchical CoMn₂O₄@Co₃O₄ core/shell nanowire arrays with the attractive electrochemical performance for SCs. However, poor electronic conductivity hinders their commercial potential use in energy storage devices.

^a Innovation Center, Faculty of Technology and Metallurgy, University of Belgrade, Karnegijeva 4, 11120 Belgrade, Serbia

^b Faculty of Technology and Metallurgy, University of Belgrade, Karnegijeva 4, 11120 Belgrade, Serbia

^c Institute for Multidisciplinary Research, University of Belgrade, Kneza Višeslava 1, 11030 Belgrade, Serbia

^d National Center for Electron Microscopy, Molecular Foundry, Lawrence Berkeley National Laboratory, Berkeley, 94720 California, United States

^e Serbian Academy of Sciences and Arts, Knez Mihailova 35, 11000 Belgrade, Serbia

† Electronic Supplementary Information (ESI) available: Fig. S1–S10, Table S1–S7. See DOI: 10.1039/x0xx00000x

Coupling spinels with a conductive matrix such as carbon fibers (CFs) could be an effective approach to address the aforementioned problem.¹² As a simple and effective technique, electrospinning enables the production of CFs/spinel composites with relatively large surface area and uniform porosity, excellent mechanical strength, high electronic conductivity and chemical stability. The most common precursor is an electrospun polyacrylonitrile (PAN) polymer owing to its good spinnability and high carbon yield.^{13,14} Recently, Abouali *et al.* successfully prepared high-performance electrospun carbon nanofiber/Co₃O₄ composites by converting as-spun cobalt acetate/PAN nanofibers via proper thermal treatment, resulting in excellent electrochemical performance.¹⁵ Similarly, various nanostructures of nickel–manganese oxides were grown on electrospun carbon fibers with high capacity values and excellent rate properties.¹⁶

Herein, we designed and prepared composite fibers made of carbon and tetragonal CoMn₂O₄ spinel nanocrystals. It can be hypothesized that such carbon–spinel coupling in composite fibers will suppress the detachment and agglomeration of nanocrystals, contributing to long-term cycling stability, without losing high capacity in aqueous electrolytes. The C@CoMn₂O₄ composite electrode demonstrated battery-type behavior, with maximum specific capacity of around 62 mAh g⁻¹ at 1 A g⁻¹ in 1 M potassium hydroxide (KOH) solution. Moreover, the electrode showed excellent stability with about 90% capacity retention after 4000 cycles at 10 A g⁻¹. It has been shown that composite fibers assembled in a symmetric coin-cell supercapacitor device could achieve maximum specific capacitance of 329 F g⁻¹ at 0.5 A g⁻¹ with excellent stability of 96.3% after 5000 consecutive cycles. To the best of our knowledge, this is the first report on such a CF@CoMn₂O₄ composite structure as a battery-type electrode material assembled in a symmetrical coin-cell device.

2. Experimental section

2.1 Materials

All chemicals were used without further purification. Polyacrylonitrile (PAN, Mw = 150 000), poly(vinylpyrrolidone) (PVP, Mw=360 000), manganese(II) acetate tetrahydrate (Mn(Ac)₂, Mw=245.09), N,N-dimethylformamide (DMF), potassium hydroxide (KOH), polytetrafluoroethylene (PTFE, 60 wt.% dispersion in water) and isopropyl alcohol (IPA, 99.5%) were purchased from Sigma Aldrich. Cobalt(II) acetate tetrahydrate (Co(Ac)₂, Mw = 249.08) and SUPER C65 conductive carbon black were purchased from Acros Organics and TIMCAL, respectively. Nickel foam substrate (NF, 99.5%) was obtained from GoodFellow. Aqueous solutions were prepared with ultrapure water of 18.2 MΩ (Milli-Q, Millipore).

2.2 Preparation of C@CoMn₂O₄ composite fibers

C@CoMn₂O₄ composite fibers were prepared by a modified procedure adopted from literature.¹⁷ In a typical synthesis, 498 mg of Co(Ac)₂ and 980 mg of Mn(Ac)₂ (molar ratio = 1:2) were

dissolved in 20 ml of DMF solution which contains 1 g of each PAN and PVP polymers. The mixture was stirred vigorously for 24 hours at room temperature. The solution was transferred to a 10 ml plastic syringe with a stainless steel needle with the inner diameter of 0.8 mm. The electrospinning process was performed at high voltage of 18 kV and a flow rate of 1 ml h⁻¹, while the distance between the nozzle and grounded copper collector was 16 cm. The as-collected electrospun fibers were placed into vacuum oven, and dried at 90 °C to remove residual DMF solvent. Subsequently, fibers were air-stabilized at 280 °C for 1 h (heating rate: 1 °C min⁻¹) and calcinated under high-purity argon atmosphere at 600 °C for 1 h (heating rate: 5 °C min⁻¹) in a tube furnace. For the sake of comparison, bare carbon fibers were prepared by following the same procedure.

2.3 Characterization

Morphology and microstructure of samples were acquired by scanning electron microscopy (SEM) performed on Tescan Mira3 XMU and FEI Helios NanoLab 660 Dual Beam System as well as (scanning) transmission electron microscopy ((S)TEM) performed on the FEI TITAN3 Themis 60–300 double aberration-corrected microscope, equipped with the super-X energy dispersive spectrometer. Crystal structure was investigated via powder X-ray diffraction (XRD) on a Bruker D8 Advance diffractometer, in the Bragg–Brentano geometry, using Cu–Kα radiation (λ=1.5406 Å) in the 2θ range of 10–70° with a step size of 0.02°. The average size (*s*) of crystals was calculated using the Debye–Scherrer equation:¹⁸

$$s = \frac{0.94 \lambda}{\beta \cos \theta} \quad (2)$$

where β is the full width at half maximum of the diffraction line. Attenuated total reflectance–Fourier transform infrared spectroscopy (ATR–FTIR, Nicolet iS10) was used to detect the functional groups in the range of 4000 cm⁻¹–400 cm⁻¹. Differential scanning calorimetry (DSC) analysis was carried out under nitrogen atmosphere up to 400 °C at the heating rate of 10 °C min⁻¹ on a Q10 instrument (TA Instruments). Thermogravimetric analysis (TGA) of as-spun fibers was carried out under air atmosphere on a Q600 analyzer (TA Instruments) up to 700 °C at the heating rate of 10 °C min⁻¹.

2.4 Electrochemical measurements

Electrochemical tests of the individual electrode were carried out in a conventional three-electrode (3E) cell configuration at room temperature. Platinum (Pt) mesh and a saturated calomel electrode (SCE) were used as the counter and reference electrode, respectively. The working electrodes were prepared by mixing a slurry composed of active materials, Super C65 and PTFE binder in isopropanol at a 8:1:1 ratio (w/w/w). The slurry was coated onto a nickel foam (NF) substrate, pressed at 10 MPa and dried at 70 °C for 12 h. Prior to coating, nickel foam was successively cleaned with acetone, 1 M HCl solution, ethanol, and deionized water in ultrasonic bath in order to remove the surface NiO layer.

The mass loading of around 2 mg cm^{-2} was determined by measuring the NF before and after coating with the active material, using an analytical balance with an accuracy of 0.01 mg. For comparison purposes, the carbon-coated NF and bare NF were also used as working electrodes. All potentials are referred to the reference electrode.

Two-electrode (2E) coin-cell devices were assembled using two identical electrode disks sandwiched by a glassy microfibre separator (GF/A, Whatman). These free-standing disks, with the mass loading of around 5 mg cm^{-2} , were punched from the vacuum dried sheet consisting of the aforementioned slurry. Prior to assembly, the electrodes were immersed in the electrolyte for 1h. Finally, the components were pressed together in a 2032 stainless steel coin cell using a crimper.

The electrochemical performance was analyzed by a Biologic potentiostat/galvanostat (SP-300 or MPG-2) workstation. Cyclic voltammetry (CV) and galvanostatic charge/discharge (GCD) experiments were performed at various sweep rates ranging from 5 to 100 mV s^{-1} and current densities from 0.5 to 12 A g^{-1} , respectively. The specific capacity of the individual electrode in the 3E cell configuration, C_s (in mAh g^{-1}), was calculated from the GCD curves using the following equation:¹⁹

$$C_s = \frac{I_d t_d}{3.6 m_e} \quad (3)$$

where I_d is the discharge current (in mA), t_d is discharge time (in s) and m_e is the mass of the electrode material (in mg). The specific capacitance of the individual electrode in the coin-cell device, $C_{s,\text{coin}}$ (in F g^{-1}), was calculated from the CV and GCD curves according to:

$$C_{s,\text{coin,CV}} = 4 \frac{\int_{V^-}^{V^+} i(V) dV}{2 \nu m \Delta V} \quad (4)$$

$$C_{s,\text{coin,GCD}} = 4 \frac{I_d t_d}{m \Delta V} \quad (5)$$

where $i(V)$ is the current of the CV loop (in mA), ν the sweep rate (in V s^{-1}), m the total mass of active electrode materials (in mg), $\Delta V = V^+ - V^-$ is the cell voltage (in V). The multiplication factor of 4 adjusts the device capacitance and the mass of two identical electrodes to the capacitance and mass of the individual electrode. The energy density (E_d , in Wh kg^{-1}) and power density (P_d , in W kg^{-1}) were calculated according to following equations:²⁰

$$E_{d,\text{CV}} = \frac{1}{3.6} \frac{1}{8} C_{s,\text{coin,CV}} \Delta V^2 \quad (6)$$

$$P_{d,\text{CV}} = \frac{3600 E_{d,\text{CV}} \nu}{\Delta V} \quad (7)$$

$$E_{d,\text{GCD}} = \frac{1}{3.6} \frac{1}{8} C_{s,\text{coin,GCD}} \Delta V^2 \quad (8)$$

$$P_{d,\text{GCD}} = \frac{3600 E_{d,\text{GCD}}}{t_d} \quad (9)$$

All calculations were done in Matlab software.

3. Results and discussion

As illustrated in Fig. 1, divalent metal ions from cobalt (in turquoise) and manganese (in blue) precursor salts are anchored on host polymers (in magenta) to form a three-dimensional (3D) network of hybrid fibers with a smooth surface (I stage), as shown by field-emission scanning electron microscopy (FE-SEM) images (Fig. 2a,b). Average diameter was calculated to be $513 \pm 101 \text{ nm}$ (Fig. 2c). As expected, bare polymer fibers exhibit a smaller average diameter of $317 \pm 53 \text{ nm}$ (Fig. 2d-f).

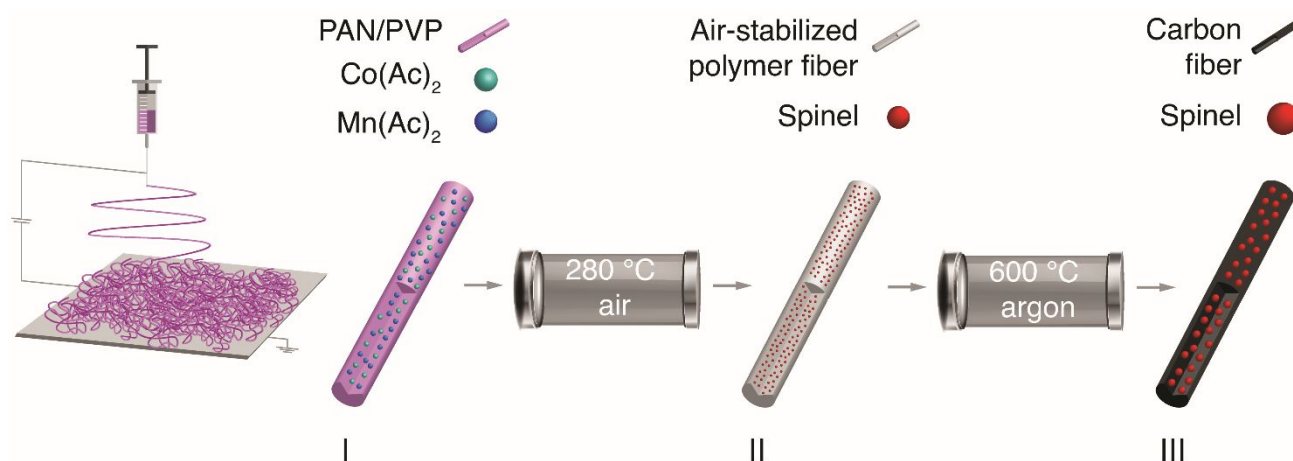


Fig. 1 Schematic illustration of C@CoMn₂O₄ composite structure formation. (I) As-spun hybrid fiber with noted cobalt (in turquoise) and manganese (in blue) precursor salts dispersed in PAN/PVP polymers (in magenta); (II) Air-stabilized polymer fiber (in gray) with Co/Mn oxide nanocrystals; (III) Composite fiber made of tetragonal CoMn₂O₄ spinel nanocrystals (in red) on carbon fiber (in black).

ARTICLE

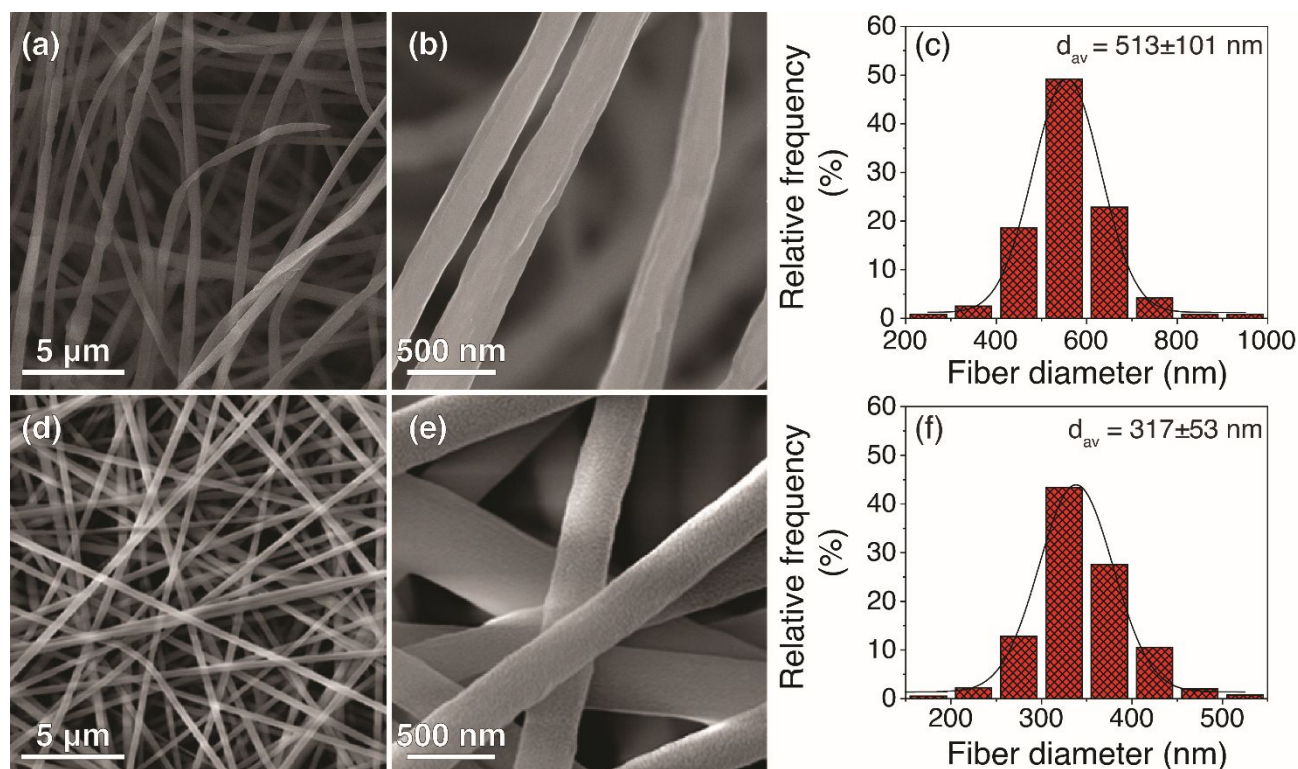


Fig. 2 FE-SEM images of as-spun hybrid fibers at different magnifications (a,b) with corresponding diameter distribution shown in (c); FE-SEM images of as-spun bare polymer fibers at different magnifications (d,e) with corresponding diameter distribution shown in (f).

ATR-FTIR transmission spectra of both, hybrid (dashed magenta line) and bare polymer fibers (black line) shown in Fig. 3a reveal characteristic vibrations for chemical groups of both polymers. The bands around 2243 and 1440 cm^{-1} can be assigned to C≡N stretching and $-\text{CH}_2-$ bending vibrations of PAN polymer, respectively. PVP exhibits bands at around 1672–1658 cm^{-1} and 1292–1290 cm^{-1} , both attributed to the stretching vibrations of C=O and C–N groups, respectively.

Hybrid fibers were converted into air-stabilized polymer fibers decorated with large amounts of small Co/Mn oxide nanoclusters using optimized thermal treatment (II stage, Fig. 1). Thermal studies were performed using differential scanning calorimetry (DSC) analysis. The DSC thermogram (Fig. 3b) of hybrid fibers exhibits a broad exothermic peak at 262 °C associated with multiple chemical reactions of oxidative stabilization, *i.e.* cyclization of the nitrile group in PAN polymer.

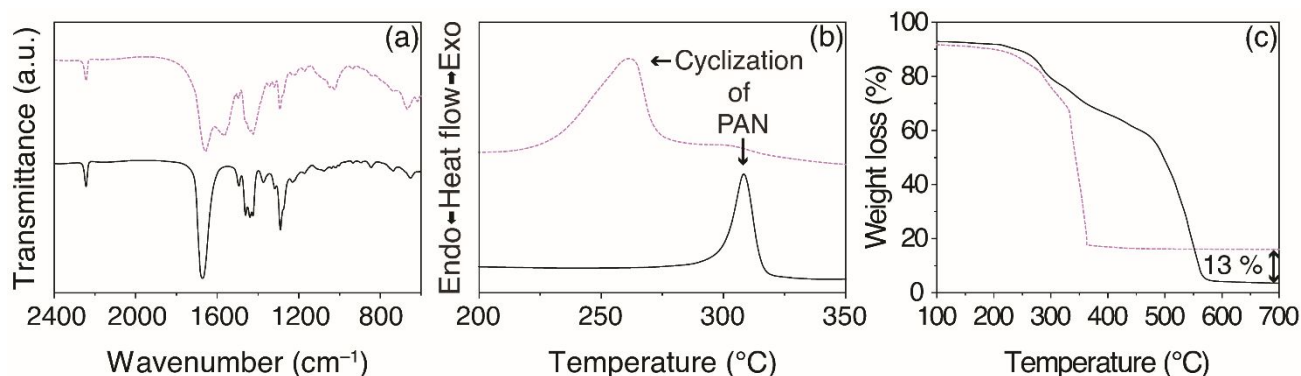


Fig. 3 ATR-FTIR spectra of as-spun hybrid (dashed magenta line) and bare polymer fibers (black line) (a) with corresponding DSC curves under nitrogen (b); and (c) TG curves under air atmosphere.

ARTICLE

The upshifted exothermic peak at 308 °C for bare polymer fibers provides evidence that metallic precursors accelerate this reaction. It has been generally accepted that after oxidative stabilization the ladder compound of heterocyclic six-membered rings is formed.²¹ The proposed structure, given in Fig. S1a, seems to have become accepted in literature, although in reality is far more complex.²² Nonetheless, it ensures the stability to higher temperature processes in which all heteroatoms are removed as various gases such as N₂, H₂, H₂O, NH₃ and HCN.²³ Accordingly, the most pronounced structural changes of air-stabilized hybrid fibers (Fig. S1b) are the reduction of the band intensities of C≡N and –CH₂– groups in the ATR–FTIR spectrum. The appearance of the broad band at around 1600 cm⁻¹ is probably due to a mix of C=N, C=C, and N–H groups which indicate that C≡N is converted into C=N.²⁴ Moreover, two bands at lower wavenumbers, *i.e.* at around 652 and 560 cm⁻¹, are likely to be associated with cobalt–oxygen/manganese–oxygen stretching vibrations.²⁵ The presence of metal oxide nanoclusters in air-stabilized fibers, was corroborated by obtained reflections from the XRD pattern (Fig. S1c), which could indicate the formation of CoMn₂O₄ spinel phase, according to JCPDS No. 01–077–0471.

In order to simulate the calcination process in air, the thermogravimetric (TG) curves of both bare polymer and hybrid fibers are shown in Fig. 3c. The polymer fibers showed four degradation steps, ≈8%, 25%, 42%, and 96% weight losses, which are present at ≈210, 328, 470, and 584 °C, respectively. The weight loss of polymer fibers is due to the removal of the residual water and DMF solvent, the PAN cyclization and removal of volatile compounds, the partial decomposition of PAN/PVP polymers side chains, and the decomposition of their main chains. Similarly, hybrid fibers exhibited three degradation steps occurring at 225, 330, and 365 °C, respectively. The weight loss of around 15% that occurred below 225 °C can be mainly attributed to the evaporation of the absorbed water and DMF solvent. The second drop in weight of around 17% in the range of 225–330 °C is due to the decomposition of the cobalt and manganese acetates in fibers, cyclization of PAN and partial decomposition of both polymers. The last step from 330 to 365 °C shows the fast decomposition of PAN and PVP polymers (≈50%) and the formation of CoMn₂O₄ crystals.^{26,27} No further apparent weight loss is observed above 400 °C, and the residual material of around 16% consists of CoMn₂O₄ crystals and carbon. The stabilized fibers were exposed to temperature of 600 °C in an inert atmosphere to derive the C@CoMn₂O₄ composite fibers (III stage, Fig. 1). The obtained reflections from the XRD pattern, given in Fig. 4, match that of JCPDS No. 00–055–0685 (noted below the pattern) which corresponds to CoMn₂O₄ tetragonal spinel phase (the unit cell is illustrated in

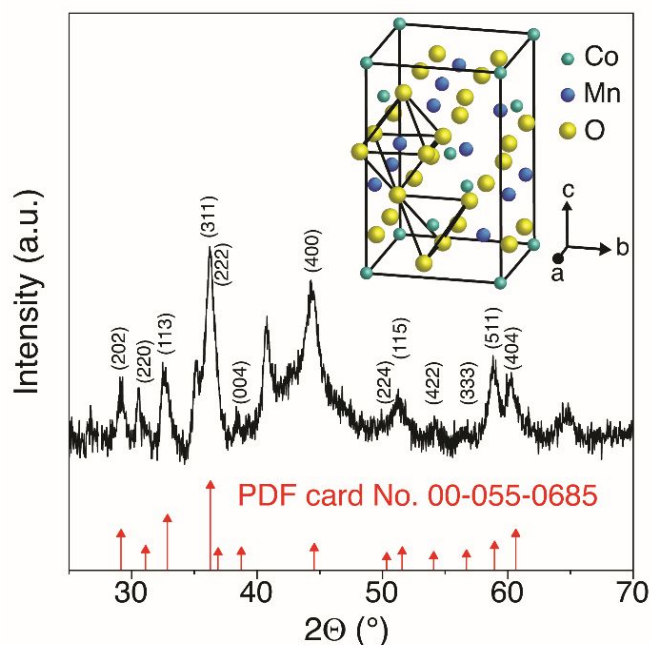


Fig. 4 XRD pattern of composite fibers compared with corresponding reference card; (inset) schematic representation of tetragonal unit cell of CoMn₂O₄ spinel structure showing Co atoms (in turquoise) occupying the tetrahedral sites, Mn atoms (in blue) placed on octahedral sites and O atoms (in yellow), respectively.

the inset of Fig. 4). The tetragonal distortion suggests the presence of high spin (*d*⁴) Jahn–Teller Mn³⁺ ions.²⁸ Moreover, MnO and Mn₃O₄ phases are also confined to a carbon structure as the side products, already observed in literature.²⁹ By using the Debye–Scherrer equation, the average size of nanocrystals was calculated to be around 18 nm.

The field–emission scanning electron microscopy (FE–SEM) images of C@CoMn₂O₄ fibers at different magnifications (Fig. 5a and b) reveal an interwoven network of randomly oriented fibers. It can be clearly seen that the CoMn₂O₄ spinel nanocrystals (white islands) are located on carbon fibers (dark grey areas). The estimated average size of nanocrystals is about 18±5 nm (Fig. S2a,b) which is in good agreement with the XRD results. The obtained small–sized spinel nanocrystals are beneficial for achieving conductive fiber composites with a highly developed surface area. The average diameter of composite fibers is found to be about 376±101 nm (Fig. S3a,b), almost twice the diameter of bare carbon fibers (Fig. S3c,d). The significant reduction of average diameter after calcination at 600 °C is probably due to weight loss and densification at higher temperatures.²⁷

ARTICLE

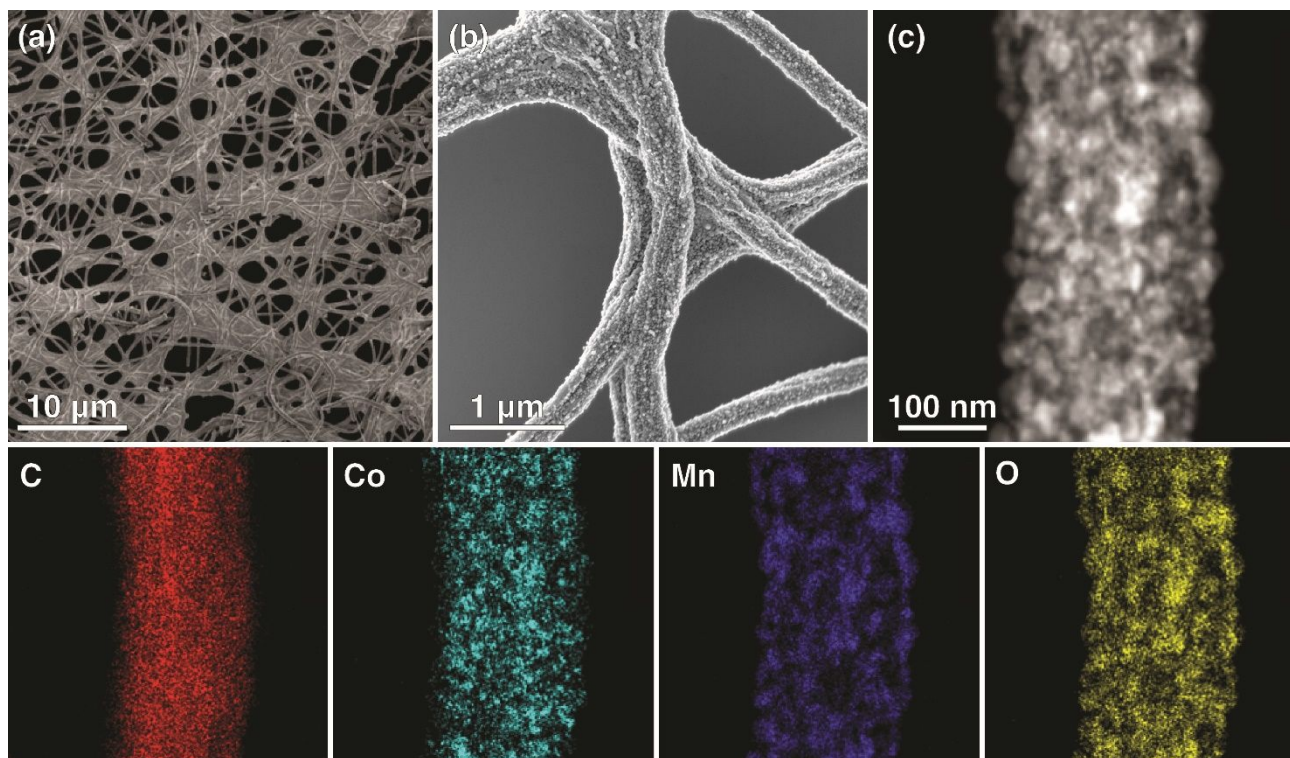


Fig. 5. (a,b) FE-SEM micrographs at different magnifications; (c) HAADF-STEM micrographs with EDX maps of C@CoMn₂O₄ noting elemental distribution of C (red), Co (turquoise), Mn (blue) and O (yellow).

Energy dispersive X-ray spectroscopy (EDS) maps obtained from scanning transmission electron microscopy high-angle annular dark field (HAADF-STEM) mode (Fig. 5c), give insight into the distribution of present chemical elements, *i.e.* carbon (C), cobalt (Co), manganese (Mn) and oxygen (O). Although average composition of spinel crystals by XRD was CoMn₂O₄, quantification of atomic percentage from EDS data (Fig. S4 and Tables S1–S3) demonstrated deviation from stoichiometry. The atomic O/(Co+Mn) ratio was estimated to be 1.29±0.09 (Table 1), lower than the theoretical ratio for the spinel CoMn₂O₄ (1.33). This oxygen deficiency is most likely due oxygen vacancies present in the structure. Interestingly, the spinel nanocrystals appear to be embedded inside the carbon fiber, corroborated by a composite EDS map (Fig. S5a,b) noting elemental distribution of C, Co and Mn. The corresponding EDS spectrum is shown in Fig. S5c.

Table 1. EDS quantification of elements in composite fibers.

O (at.%)	Co (at.%)	Mn (at.%)	O/(Co +Mn)
12.02±3.94	3.30±1.76	6.17±1.87	1.29±0.09

Conventional transmission electron micrograph (CTEM) of a composite fiber is seen in Fig. 6a. Experimental parallel beam electron diffraction pattern taken close to [0 -1 1] zone axis (Fig. 6b) of crystal (zero spot is covered by the beam stop), 111 facet of which is noted by arrow in Fig. 6a corresponds to simulated diffraction pattern (Fig 6c) of cubic MnO, (225) Fm-3m in [0 -1 1] zone axis, seen from noted 111 and 200 reflections. This corroborates XRD findings that there is MnO phase present in the system along with quantification of EDS data of particle which notes almost 1:1 at.% ratio of Mn and O, with negligible presence of Co (Table S4).

ARTICLE

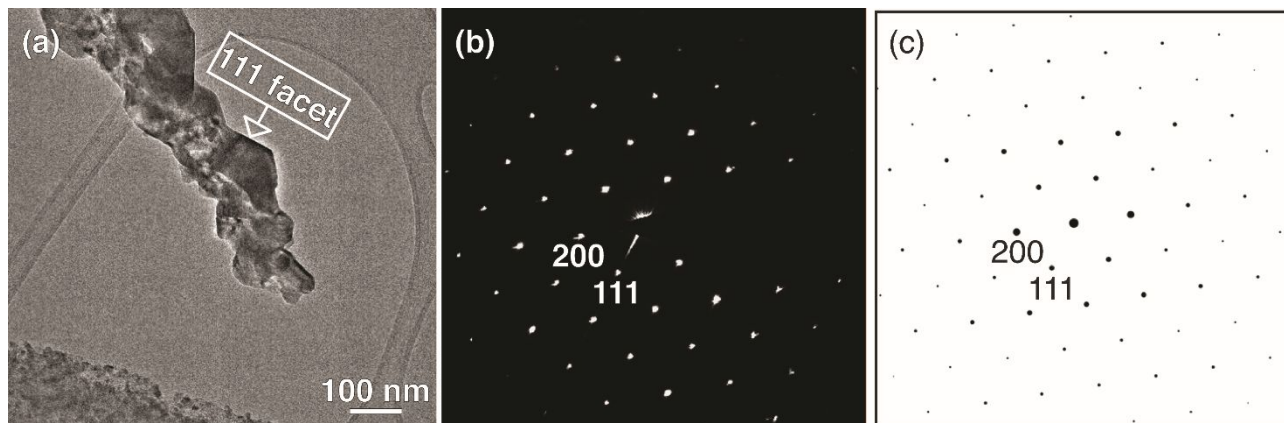
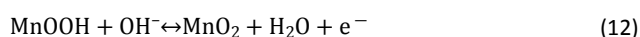
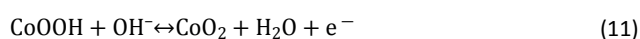


Fig. 6. (a) CTEM micrograph of single C@CoMn₂O₄ composite fiber with noted 111 facet of nanocrystal; (b) diffraction pattern of noted nanocrystal; (c) simulated diffraction pattern of cubic MnO, space group (225) Fm-3m.

The electrochemical performance of as-prepared composite fibers was initially evaluated using a conventional three-electrode (3E) system. Fig. 7a presents the CV curves at various sweep rates in a potential range of 0–0.5 V, vs. SCE. Evidently, the shape of the CV curves, indicates the presence of faradaic redox processes which can be described with following reactions (10–12):³⁰



The anodic peak potentials for the reactions of Co²⁺/Co³⁺ (equation (10)) and Co³⁺/Co⁴⁺ (equation (11)) are reported to be very close to each other, thus, only one anodic peak emerged within 0.39–0.43 V vs. SCE. The cathodic peak potentials at around 0.10 V, pronounced at lower sweep rates (Fig. 7b, black line), and around 0.15–0.21 V vs. SCE can be ascribed to their corresponding reduction processes.³¹ Notably, the voltammetric currents of nickel foam substrate are negligible in the examined potential range (Fig. 7b, red line), thus, the main contribution to the current response could be ascribed to C@CoMn₂O₄ composite electrode. Moreover, the voltammetric currents of bare carbon fibers are significantly lower than those of the composite electrode (Fig. 7b, blue line).

In order to separate the contributions of capacitive and diffusion-controlled currents from the total current, we used a method derived from Conway *et al.*³² and Dunn *et al.*³³. Accordingly, it can be estimated that the current at a fixed potential, $i(V)$, represents the sum of both surface capacitive

effects (k_1v) and diffusion-controlled processes ($k_2v^{1/2}$) according to the following equation:

$$i(V) = k_1v + k_2v^{1/2} \quad (13)$$

where k_1 and k_2 are proportionality constants independent of the sweep rate, v . The equation (13) can be further rewritten as:

$$i(V)/v^{1/2} = k_1v^{1/2} + k_2 \quad (14)$$

Using the aforementioned equations, it is possible to determine both constants, *i.e.* k_1 and k_2 , as the slope and the intercept of the fitted plot $i(V)/v^{1/2}$ vs. $v^{1/2}$, respectively. The procedure is given in more detail in ESI. The dashed area of CV curve at sweep rate of 5 mV s⁻¹, shown in Fig. 7c, represents the capacitive contribution, which is around 70% of the total stored charge.

Furthermore, galvanostatic charge/discharge (GCD) measurements of composite electrode were performed. GCD curves with the plateaus could be observed especially at lower current densities (Fig. 7d), which is an indication of the battery-type behavior. Consequently, the most appropriate metric to evaluate the performance is the specific capacity expressed in mAh g⁻¹.^{34,35} Using the calculation outlined in the experimental section, the highest value of specific capacity was found to be around 62 mAh g⁻¹ at a current density of 1 A g⁻¹. When the current density was increased to 10 A g⁻¹, the specific capacity remained at about 58% of the initial value (Fig. 7e and Table S5). Taking into account the mass loadings of active materials, the values are higher than the specific capacity of various recently reported transition metal oxide-based electrodes (Table S6).

ARTICLE

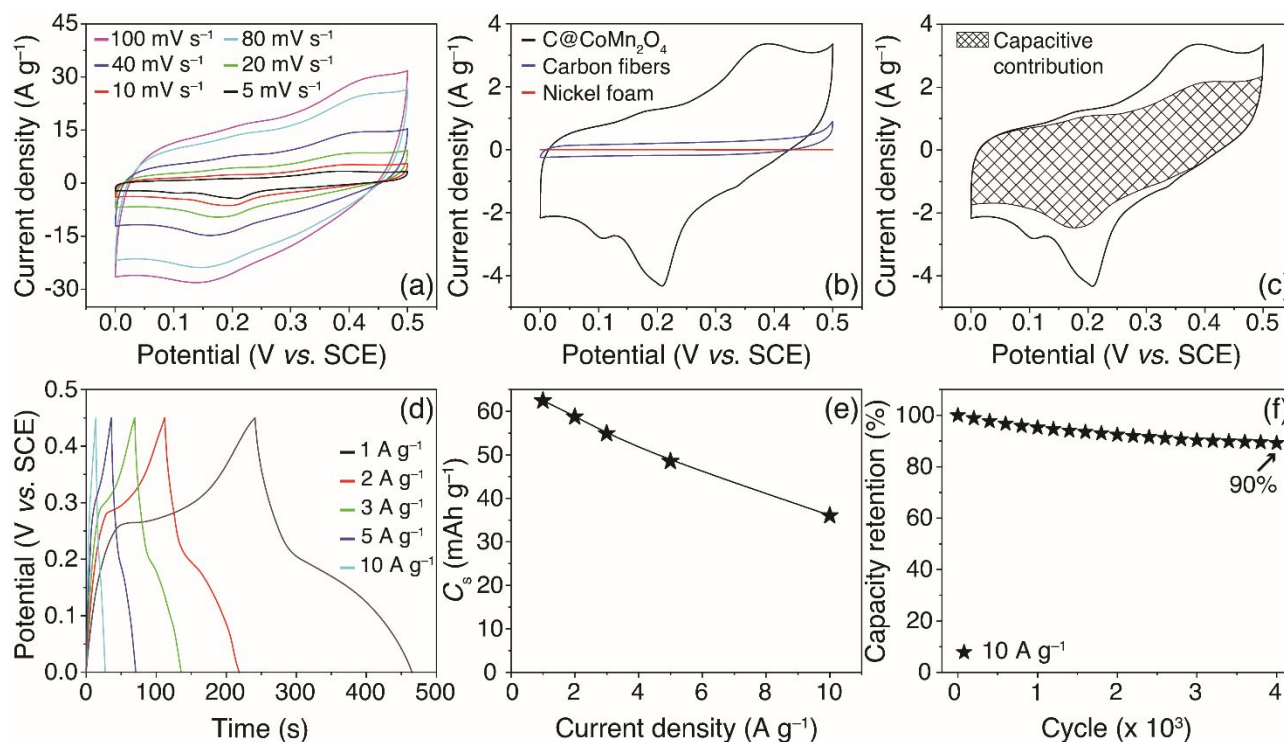


Fig. 7. (a) CV curves of C@CoMn₂O₄ composite electrode at various sweep rates (noted in the figure); (b) CV curves of composite fibers (black), bare carbon fibers (blue) and nickel foam (red) at sweep rate of 5 mV s⁻¹; (c) charge separation curves (the hashed area noting the capacitive contribution derived from Dunn's method); (d) charge/discharge profiles at various current densities; (e) specific capacities at different current densities; (f) capacity retention obtained by cycling composite electrode at current density of 10 A g⁻¹.

For example, pure spinels, CoMn₂O₄ (around 34.5 mAh g⁻¹)³⁶, Co₂MnO₄ (around 50.0 mAh g⁻¹)³⁷, CuCo₂O₄ (around 44.0 mAh g⁻¹)³⁸ and various spinel-based composite electrodes, such as Co₂MnO₄@VCFs (around 48.4 mAh g⁻¹)³⁹, ZnFe₂O₄@porous activated carbon fibers (around 58 mAh g⁻¹ at 1 A g⁻¹)⁴⁰, Co₃O₄@carbon nanofibers (around 43 and 48 mAh g⁻¹ at 1 A g⁻¹)¹⁵, Fe₃O₄@carbon nanotubes (around 39 mAh g⁻¹ at 1 A g⁻¹)⁴¹ etc. The given literature values were converted into mA h g⁻¹ from F g⁻¹ unit, using the equation (3).

The cycle performance is very important for supercapacitor applications, thus, the capacity retention of composite electrode tested at a current density of 10 A g⁻¹ is shown in Fig. 7f. Importantly, the electrode retained 90% of its initial specific capacity at the high current density, showing very good electrochemical stability. This result can be ascribed to the preserved structure after long-term cycling, shown in SEM micrograph recorded after 4000 cycles (Fig. S7), which can be explained by strong coupling between spinel nanocrystals and carbon fibers.

To investigate the practical application of C@CoMn₂O₄ composite fibers, symmetrical coin-cell devices were assembled. As it is expected for symmetrical 2E system, quasi-rectangular CV loops in the voltage range 0.0 V–0.8 V were obtained, shown in Fig. 8a, suggesting low contact resistance of the device. To estimate the energy storage capacity and rate capability of composite electrode, CV data are obtained at various sweep rates ranging from 5 to 100 mV s⁻¹ (noted in the figure). Quantitatively, C@CoMn₂O₄ exhibited the specific capacitance of 277 F g⁻¹ at a sweep rate of 5 mV s⁻¹, which is around 11.5 times higher than that of bare carbon fibers at the same sweep rate (Fig. 8b). Moreover, the composite electrode retained a capacitance value of 137 F g⁻¹ at a sweep rate of 100 mV s⁻¹, suggesting good rate capability of about 50%.

GCD curves recorded at different current densities in the voltage range 0.0–0.8 V are shown in Fig. 8c. The shape of these curves indicates the existence of faradaic reactions. The maximum specific capacitance of composite fibers reaches 329 F g⁻¹ at 0.5 A g⁻¹, as seen in Fig. 8d, which is around 13 times

ARTICLE

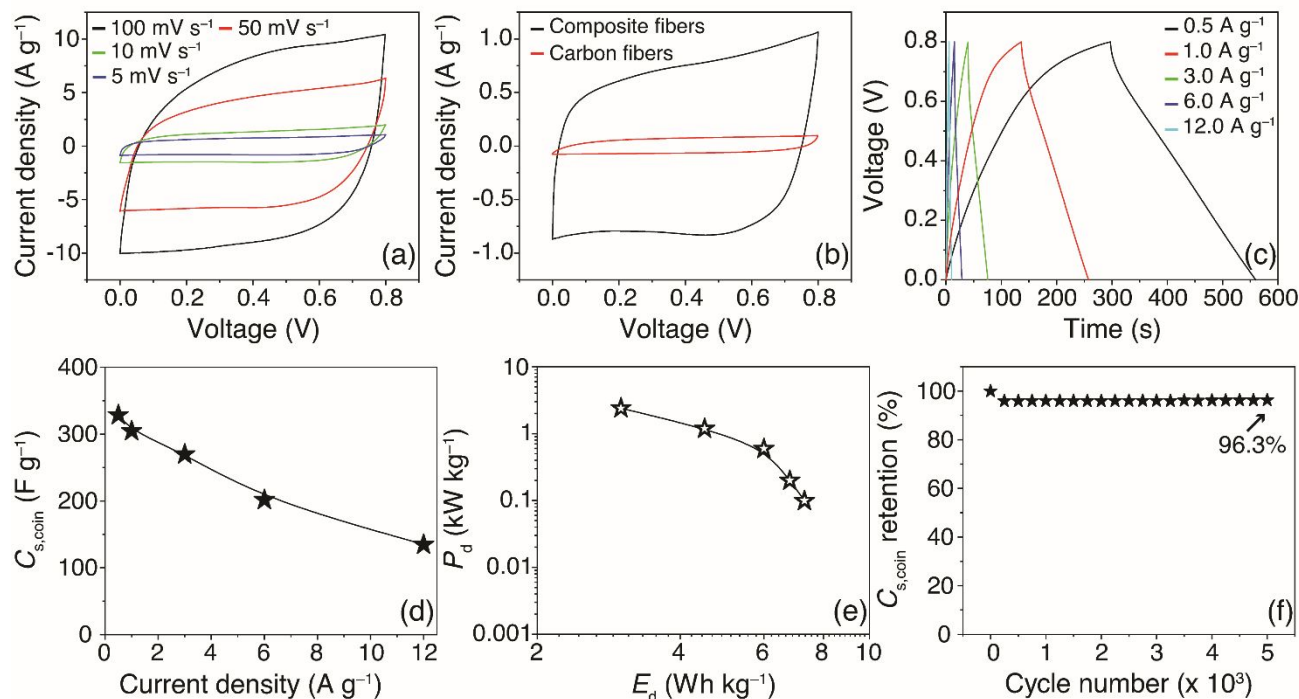


Fig. 8. (a) CV curves recorded at various sweep rates for C@CoMn₂O₄ in the coin-cell device; (b) comparison of CV curves for composite (black line) and bare carbon fibers (red line) at a sweep rate of 5 mV s⁻¹; (c) GCD curves at various current densities; (d) rate performance; (e) Ragone plot; and (f) capacitance retention obtained by cycling coin-cell device at a sweep rate of 100 mV s⁻¹.

higher than that of bare carbon fibers (Fig. S8). When the current density is increased by 24-fold, C@CoMn₂O₄ still exhibits 135 F g⁻¹. The energy and power densities of the coin-cell device were calculated, and the corresponding Ragone plot is shown in Fig. 8e. Notably, the maximum energy density is estimated to be around 7.3 Wh kg⁻¹ at a power density of 0.1 kW kg⁻¹. Even at a power density of 2.4 kW kg⁻¹, the energy density of 3.0 Wh kg⁻¹ can be considered relatively high.

The stability of the coin-cell devices was evaluated by conducting CV measurements for 5000 consecutive cycles at a sweep rate of 100 mV s⁻¹. The capacitance dependence of cycle number is presented in Fig. 8f. Excellent cycle life of the composite electrode was observed, with 96.3% retention of its initial capacitance after 5000 cycles. The long-term stability of composite fibers is superior to some recent reports for similar systems^{15,42,43} which is very promising from the application standpoint.

Conclusions

We employed a facile strategy to produce composite fibers made of carbon and CoMn₂O₄ spinel nanocrystals. Electrospun hybrid fibers were calcinated in argon in order to develop composite structure which was comprehensively characterized by XRD, SEM, CTEM, STEM and EDS analyses. Synergy of both components, spinel nanocrystals and carbon, due to strong electrical and chemical coupling, yields a composite electrode which exhibits excellent electrochemical properties in aqueous systems. The electrode delivered high specific capacity of 62 mAh g⁻¹, excellent rate capability and cycling stability of 90% after 4000 consecutive charge/discharge cycles. A symmetrical coin-cell device was further assembled, exploiting C@CoMn₂O₄ composite fibers as an electrode, which delivered high energy density of 7.3 Wh kg⁻¹ at a power density of 0.1 kW kg⁻¹ and long-term cycling stability (96.3% retention after 5000 cycles) showing potential for practical applications.

Conflicts of interest

There are no conflicts to declare.

Acknowledgements

This work was supported by the Ministry of Education, Science and Technological Development of the Republic of Serbia (Contract No. 451-03-9/2021-14/200135). V.R. Radmilović acknowledges support from the Serbian Academy of Sciences and Arts under project no. F-141. Work at the Molecular Foundry was supported by the Office of Science, Office of Basic Energy Sciences, of the U.S. Department of Energy under Contract No. DE-AC02-05CH11231.

References

- B.E. Conway, *Electrochemical Supercapacitors: Scientific Fundamentals and Technological Applications*, Springer, New York, 1999.
- P. Simon and Y. Gogotsi, *Nat. Mater.*, 2020, **19**, 1151–1163.
- F. Beguin, V. Presser, A. Balducci and E. Frackowiak, *Adv. Mater.*, 2014, **26**, 2219–2251.
- Y.-Z. Zhang, T. Cheng, Y. Wang, W.-Y. Lai, H. Pang and W. Huang, *Adv. Mater.*, 2016, **28**, 5242–5248.
- Y.-Z. Zhang, Y. Wang, T. Cheng, L.-Q. Yao, X. Li, W.-Y. Lai and W. Huang, *Chem. Soc. Rev.*, 2019, **48**, 3229–3264.
- Q. Zhao, Z. Yan, C. Chen and J. Chen, *Chem. Rev.*, 2017, **117**, 10121–10211.
- S. Meng, Y. Wang, Y. Zhang, Q. Xu, D. Jiang and M. Chen, *CrystEngComm*, 2020, **22**, 6864–6875.
- S. Peng, L. Li, Y. Hu, M. Srinivasan, F. Cheng, J. Chen and S. Ramakrishna, *ACS Nano*, 2015, **9**, 1945–1954.
- Y. Xu, X. Wang, C. An, Y. Wang, L. Jiao and H. Yuan, *J. Mater. Chem. A*, 2014, **2**, 16480–16488.
- S. Liu, D. Ni, H.-F. Li, K. N. Hui, C.-Y. Ouyang and S. C. Jun, *J. Mater. Chem. A*, 2018, **6**, 10674–10685.
- X. Chen, X. Liu, Y. Liu, Y. Zhu, G. Zhuang, W. Zheng, Z. Cai and P. Yang, *RSC Adv.*, 2018, **8**, 31594–31602.
- J. Liang, H. Zhao, L. Yue, G. Fan, T. Li, S. Lu, G. Chen, S. Gao, A.M. Asiri and X. Sun, *J. Mater. Chem. A*, 2020, **8**, 16747–16789.
- M. Kopeć, M. Lamson, R. Yuan, C. Tang, M. Kruk, M. Zhong, K. Matyjaszewski and T. Kowalewski, *Prog. Polym. Sci.*, 2019, **92**, 89–134.
- X. Zhang, T. Kitao, D. Piga, R. Hongu, S. Bracco, A. Comotti, P. Sozzani and T. Uemura, *Chem. Sci.*, 2020, **11**, 10844–10849.
- S. Abouali, M.A. Garakani, B. Zhang, Z.-L. Xu, E. Kamali Heidari, J.-q. Huang, J. Huang and J.-K. Kim, *ACS Appl. Mater. Interfaces*, 2015, **7**, 13503–13511.
- D. Tian, X. Lu, G. Nie, M. Gao and C. Wang, *Inorg. Chem. Front.*, 2018, **5**, 635–642.
- D.M. Mijailović, V.V. Radmilović, U.Č. Lačnjevac, D.B. Stojanović, V.D. Jović, V.R. Radmilović and P.S. Uskoković, *Appl. Surf. Sci.*, 2020, **534**, 147678.
- H.P. Klug and L. E. Alexander, *X-ray diffraction procedures: For polycrystalline and amorphous materials*, John Wiley & Sons, 1974.
- Y. Gogotsi and R.M. Penner, *ACS Nano*, 2018, **12**, 2081–2083.
- E. Mourad, L. Coustan, P. Lannelongue, D. Zigah, A. Mehdi, A. Vioux, S.A. Freunberger, F. Favier and O. Fontaine, *Nat. Mater.*, 2017, **16**, 446–453.
- S. Peng, L. Li, J.K.Y. Lee, L. Tian, M. Srinivasan, S. Adams and S. Ramakrishna, *Nano Energy*, 2016, **22**, 361–395.
- B. Saha and G.C. Schatz, *J. Phys. Chem. B*, 2012, **116**, 4684–4692.
- M.S.A. Rahaman, A. F. Ismail and A. Mustafa, *Polym. Degrad. Stab.*, 2007, **92**, 1421–1432.
- S.N. Arshad, M. Naraghi and I. Chasiotis, *Carbon*, 2011, **49**, 1710–1719.
- P.W. Menezes, A. Indra, N.R. Sahraie, A. Bergmann, P. Strasser and M. Driess, *ChemSusChem*, 2015, **8**, 164–171.
- J. Bhagwan, V. Sivasankaran, K.L. Yadav and Y. Sharma, *J. Power Sources*, 2016, **327**, 29–37.
- H. Zhu, D. Yu, S. Zhang, J. Chen, W. Wu, M. Wan, L. Wang, M. Zhang and M. Du, *Small*, 2017, **13**, 1700468.
- F. Cheng, J. Shen, B. Peng, Y. Pan, Z. Tao and J. Chen, *Nat. Chem.*, 2011, **3**, 79–84.
- L. Ji, A.J. Medford and X. Zhang, *J. Mater. Chem.*, 2009, **19**, 5593–5601.
- F. Yunyun, L. Xu, Z. Wankun, Z. Yuxuan, Y. Yunhan, Q. Honglin, X. Xuetao and W. Fan, *Appl. Surf. Sci.*, 2015, **357**, 2013–2021.
- F. Zhang, C. Yuan, J. Zhu, J. Wang, X. Zhang and X.W. (David) Lou, *Adv. Funct. Mater.*, 2013, **23**, 3909–3915.
- T.C. Liu, W.G. Pell, B. E. Conway and S. L. Roberson, *J. Electrochem. Soc.*, 1998, **145**, 1882–1888.
- J. Wang, J. Polleux, J. Lim and B. Dunn, *J. Phys. Chem. C*, 2007, **111**, 14925–14931.
- T.S. Mathis, N. Kurra, X. Wang, D. Pinto, P. Simon and Y. Gogotsi, *Adv. Energy Mater.*, 2019, **9**, 1902007.
- T. Brousse, D. Belanger and J.W. Long, *J. Electrochem. Soc.*, 2015, **162**, A5185–A5189.
- N. Kanaujia, N. Kumar, M. Singh, Y. Sharma and G.D. Varma, *J. Energy Storage*, 2021, **35**, 102302.
- L. Li, Y.Q. Zhang, X.Y. Liu, S.J. Shi, X.Y. Zhao, H. Zhang, X. Ge, G.F. Cai, C.D. Gu, X.L. Wang and J.P. Tu, *Electrochim. Acta*, 2014, **116**, 467–474.
- A. Pendashteh, M.S. Rahmanifar, R.B. Kaner and M.F. Mousavi, *Chem. Commun.*, 2014, **50**, 1972–1975.
- M. Nagaraju, S.C. Sekhar, S.J. Arbaz and J.S. Yu, *Appl. Surf. Sci.*, 2021, **563**, 150223.
- S. Yang, Z. Han, F. Zheng, J. Sun, Z. Qiao, X. Yang, L. Li, C. Li, X. Song and B. Cao, *Carbon*, 2018, **134**, 15–21.
- D. Guan, Z. Gao, W. Yang, J. Wang, Y. Yuan, B. Wang, M. Zhang and L. Liu, *Mater. Sci. Eng. B*, 2013, **178**, 736–743.
- M. Liu, M. Shi, W. Lu, D. Zhu, L. Li and L. Gan, *Chem. Eng. J.*, 2017, **313**, 518–526.
- B. Pant, M. Park, G. P. Ojha, J. Park, Y.-S. Kuk, E.-J. Lee, H.-Y. Kim and S.-J. Park, *J. Colloid Interface Sci.*, 2018, **522**, 40–47.